Journal of Materials Chemistry C

Accepted Manuscript

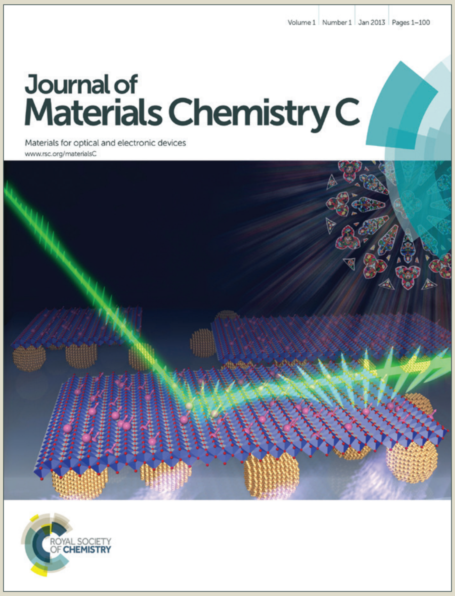

Journal of Materials Chemistry C RSCPublishing

Paper

Cite this: DOI: 10.1039/x0xx00000x

Received 00th January 2014,
Accepted 00th January 2014

DOI: 10.1039/x0xx00000x

www.rsc.org/

Simulation and Prediction of the Thermal Sintering Behavior for a Silver Nanoparticle Ink Based on Experimental Input

Sebastian Wünscher,[1,2]‡ Tobias Rasp,[3]‡ Michael Grouchko,[4] Alexander Kamyshny,[4] Renzo M. Paulus,[1,2] Jolke Perelaer,[1,2,5]* Torsten Kraft,[3] Shlomo Magdassi,[4] Ulrich S. Schubert[1,2,5]*

In order to develop a prediction model for resistivity evolution during isothermal sintering, a commercial silver nanoparticle ink was characterized for its metal content, particle size and behavior upon heating. Electrical properties, mass loss behavior, grain size development and material densification were studied for thermal sintering at 175 °C. The correlation between mass loss, height loss of the resulting sintered structures, grain size and electrical resistivity was investigated to gain further understanding of the silver nanoparticle sintering process. The results of thermal sintering were used to calibrate a discrete element sintering model that provides microstructural properties with which the resistivity development at 150 and 200 °C was successfully predicted. The model was validated by experimental data obtained at these temperatures. A variation of particle size and particle size distribution in the simulations furthermore illustrate their influence on final resistivity showing that using small particles with a broad distribution are preferable for reducing the final resistivity of the inkjet-printed pattern.

1. Introduction

In the field of flexible electronics, inkjet printing has become a frequently used patterning technique to deposit various functional materials.[1, 2] As digital and additive manufacturing method, drop-on-demand (DOD) inkjet printing offers several advantages compared to vapor deposition and other solution based manufacturing methods.[1] It offers design flexibility without the requirement of masks, the deposition of several layers of different materials in different printing resolution in the same printing process, an efficient handling of expensive materials due to its minimal waste production and the potential to be integrated in roll-to-roll (R2R) manufacturing.[1, 3, 4] One particular research focus of inkjet printing is the fabrication of electrically conductive structures on flexible substrates,[5] which can be used as contacts, electrodes, interconnects and antenna structures in radio frequency identification (RFID) tags,[6] organic photovoltaics (OPV),[7] organic light emitting diodes (OLED),[8] thin film transistors (TFT),[9] molecular diagnostic devices[10] and applications for electromagnetic shielding, such as frequency selective surfaces (FSS).[11]

For the preparation of conductive features, three types of metal-based inks have been frequently reported in the literature: An ink can contain either metal organic decomposition (MOD) complexes,[12] a metal salt[13] or metallic nanoparticles (NPs).[14] Whereas the first two types of inks do not contain particles and behave as a solution, their advantage is being easy to print. However, these inks usually suffer from a low metal loading (< 30 wt%). Typical metals that are used are gold,[15] silver[5] and copper.[16] NP-based inks contain NPs with a diameter preferably below 50 nm, which are dispersed in water or organic solvent and have a metal loading in the range of 20 to 70 wt%.[5, 17] To avoid agglomeration of metal particles and nozzle clogging during inkjet printing, stabilizing molecules are added to the ink formulation.[16] Stabilizers like polymers (polyacrylic acid, polyvinylpyrolidone) or low molar mass molecules (long chained thiols and carboxylates) attach to the individual particles with their polar anchoring groups. Their bulky polymer backbone or long alkyl chain causes steric stabilization, or if charged, electrostatic and/or electrosteric stabilization of the dispersed metal particles.[16-18]

After ink deposition, however, the stabilizers act as an insulating organic shell around each particle and, therefore, prevent electrical conductivity of the printed pattern. To achieve conductive patterns, the organic stabilizer has to be removed from the particles in order to

---

1 Laboratory of Organic and Macromolecular Chemistry (IOMC), Friedrich Schiller University Jena, Humboldtstr. 10, 07743 Jena, Germany.
2 Jena Center for Soft Matter (JCSM), Friedrich Schiller University Jena, Philosophenweg 7, 07743 Jena, Germany.
3 Fraunhofer Institute for Mechanics of Materials (IWM), Wöhlerstraße 11, 79108 Freiburg, Germany.
4 Casali Institute for Applied Chemistry, Institute of Chemistry, The Hebrew University of Jerusalem, Jerusalem 91904, Israel.
5 Dutch Polymer Institute (DPI), P.O. Box 513, 5600 MB Eindhoven, The Netherlands.

‡ Both authors contributed equally to the presented work.

† Electronic Supplementary Information (ESI) available: See DOI: 10.1039/b000000x/

Email: ulrich.schubert@uni-jena.de; jolke.perelaer@uni-jena.de;

bring them in direct physical contact. This process can be divided in two stages. In the first stage, the organic coating is removed from the metal NP at the curing temperature.[18] At this stage the metal particles make direct contact and have a relatively low conductance. In the second stage, larger particles are formed at the expense of smaller particles due to grain growth, sintering (merging without melting) and Ostwald ripening.[19] As a result, a reduction of surface energy will take place, followed by a mass flow to increase the neck radii and particle growth.[20] The complete removal of the stabilizers is typically achieved by decomposing the stabilizer by the application of temperatures above 200 °C.[21] However, for printed electronic applications cost-effective and flexible polymer substrates are used, such as polycarbonate and polyethylene naphthalate, that have a glass transition temperature (Tg) well below the sintering temperature of the metal precursor ink. The high temperature that is required for the sintering may then (permanently) damage the substrate. It is therefore crucial that the processing temperature remains below the Tg of the substrate.

In order to decrease the thermal impact on the polymer substrate, two main strategies were developed in recent years. The first approach is the use of alternative sintering techniques such as microwave sintering,[22] plasma sintering,[23, 24] electrical sintering,[25] laser sintering[26] or photonic flash sintering.[27] These techniques are capable of inserting a sufficient amount of energy to sinter printed patterns formed by metallic NPs without affecting the underlying polymer substrate.[4] A second approach is to tailor the ink formulation revealing a sintering temperature that is compatible with the Tg of the polymer substrate. Despite that metallic NPs reveal a reduced melting temperature compared to their bulk material,[28] the organic stabilizing agent prevents a low sintering temperature.[29] Consequently, the stabilizing agent introduces a balance between the NP dispersion stability, ink printability and its ability to be sintered.[30] Several groups have focused on room temperature sintering by the addition of so called sintering agents. Solvents like methanol were used to dissolve the stabilizing molecules and remove them from the printed patterns.[31] Also removal of thiol stabilizers from a gold NP-based ink by oxidation *via* nitrogen dioxide was reported.[32] After chemical removal of the stabilizers, coalescence of the naked particles and rising electrical conductivity was observed. Another chemical sintering approach is the addition of electrolytes (halides, polyelectrolytes) to printed silver NP-based inks in order to replace the stabilizing molecules on the surface of each particle and to reduce the steric repulsion that causes spontaneous coalescence of NPs.[33-35] These approaches show that electrical conductivity can be achieved without the complete removal of the stabilizers from a printed silver NP ink. Mechanistic studies on a thiol stabilized silver NPs ink revealed that thermal annealing well below the decomposition temperatures of the stabilizers also results in electrically conductive patterns.[36] It was reported that the thiol stabilizers detach from the silver particles and sintering occurs whilst the organics are present in the printed pattern.

For the optimization of metal precursor inks with respect to their ability to be sintered at low temperatures yielding highly conductive patterns, an exact understanding of the sintering mechanism is required. Deriving a sintering and a resistivity prediction model from basic experimental data represents therefore an essential tool to gain further insights into the sintering mechanism. Simulation of the coalescence of gold and silver NPs was performed on the basis of the Embedded Atom Method (EAM).[37, 38] These models, however, consider only the interaction of a small number of particles in order to provide a detailed understanding of the coalescence mechanisms. As a result, these models cannot provide a resistivity model for inkjet-printed patterns. A resistivity simulation allows the alteration of more difficult accessible parameters, like particle size and particle size distribution, and their effects on the obtainable resistivity of the printed patterns at different sintering conditions.

As the resistivity of an inkjet-printed line is defined by its microstructural composition, it is reasonable to use a particle-based method like the Discrete Element Method (DEM)[39] to simulate the sintering process. This method considers each silver grain in the ink as a distinct particle that interacts with neighboring grains by appropriate sintering force laws. In contrast to continuum mechanical approaches, the DEM enables the analysis of the developing particle arrangement during sintering and fundamental microstructural properties, like coordination number and contact radius, can be tracked.[40] Sintering simulations of thin films on a substrate using DEM have been compared with experiments regarding densification[41] and film shrinkage,[42] but without a determination of the connected particle paths through the sample, which is essential for the resistivity computation. Schneider *et al*.[43] have estimated the effective conductivity in a solid oxide fuel cell electrode represented by a sintered particle assembly by substituting each particle contact with an appropriate resistance leading to a resistance network. The resulting conductivity is determined by imposing potentials at the particles that define the electrolyte and current collector, while applying Kirchhoff's current law and resistance Ohm's law.

In this contribution, we present our developments of a new phenomenological model for computing the resistivity evolution during thermal sintering of inkjet-printed lines that is derived from experimental results of a commercial silver NP ink. Subsequently, we verify the modeling output at various sintering temperatures with experimental data. The resulting model was also used to compute the influence of the particle size and particle size distribution to the final resistivity. The sintering conditions applied in this research, however, are partially in disagreement with other requirements such as the use of heat sensitive polymeric substrates that allow sintering only up to certain temperatures. Particularly because a compromise between preferable sintering conditions and feasible production requirements has to be found, a prediction model for resistivity is a prerequisite for testing several processing combinations in a comfortable and economical way.

2. Experimental procedure

2.1 Inkjet printing and sintering

For inkjet printing, an aqueous dispersion of silver NPs was purchased (X-Jet Solar, Israel). This silver ink contains 30 wt% of silver NPs with an average particle radius of 10 nm. Inkjet printing was performed using a Dimatix DMP 2800 system (Dimatix-Fujifilm Inc., USA), equipped with a 10 pL cartridge (DMC-11610). The dispersion was printed at a voltage of 25 V, using a frequency of 9 kHz and a customized waveform. The printing height was set to 1 mm, while using a dot spacing of 21 µm. Printing was performed at room temperature in order to suppress coffee ring effects in the deposited features. The printed test pattern contains five lines of a length of 15 mm for each sample with a distance of 3 mm to each other. For thermal sintering studies, standard microscopy glass slides (75×25 mm^2, Carl Roth GmbH + Ko. KG, Karlsruhe, Germany) were used. All substrates were cleaned prior to printing by rinsing with isopropanol and dried under a flow of nitrogen. Thermal sintering was carried out immediately after printing on a hot-plate at 150 °C, 175 °C and 200 °C for up to 60 min. Height loss investigations were performed in a similar manner. A sample of five inkjet-printed lines was heated on a hotplate. The height of the sample was measured after defined time intervals (every minute in the first 10 minutes of sintering) at the respective sintering temperature.

2.2 Characterization methods

Thermogravimetric analyses (TGA) were performed using a TG50 by Mettler Toledo (Greifensee, Switzerland) under ambient atmosphere in the range from 25 to 350 °C with a heating rate of 10 K min^{-1}. Isothermal TGA was performed at 150 °C, 175 °C and 200 °C for up to three hours. The ink was pre-dried with a drying procedure containing heating at 60 °C for 30 min and vacuum drying for 30 min at a pressure of 0.4 mbar.

Resistance investigations were performed via 2-point measurements using a multimeter (Voltcraft Digital Multimeter VC-960, Conrad Electronics GmbH, Germany). The electrodes were attached to conductive pads from a conductive silver paste (Conrad Electronics GmbH, Germany) on each side of a printed line. Surface topography, thickness and cross-sectional areas of the printed silver lines were measured with an optical profilometer (Wyko NT9100, Veeco, Mannheim, Germany). Resistivity was calculated from the cross-sectional area A, the line length l and the resistance R of each line using $\rho = RA/l$. High resolution scanning electron microscopy (HR-SEM) images were taken using a Gemini 1530 type LEO field-emission scanning electron microscope (Carl-Zeiss AG, Germany). The lines were printed on pre-damaged microscopy glass slides and broken after sintering. Evaluation of particle size by dynamic light scattering (DLS) was performed using Zetasizer Nano ZS (Malvern Instruments, UK).

3. Modeling

The model for computing the resistivity was split in two stages. In the first stage, the sintering process of the line is simulated by a particle-based method whereas in the second stage, the resistivity is computed with the help of specific parameters that can be extracted from the process simulation of the first stage.

3.1 Process simulation

After drying, an inkjet-printed line remains as an aggregate of metallic particles and non-conductive organics. To account for this specific structure, it is reasonable to apply a particle-based method like the Discrete Element Method (DEM) to simulate the subsequent sintering step. The DEM is a simulation method for which each grain is regarded as a distinct particle that interacts with neighboring particles by given force laws. All particles are defined by their position and radius. Every single particle is considered free in translational and rotational motion. Therefore, processes taking place on the nano-scale, like particle rearrangement and contact formation, can be followed and the evolution of microstructural properties, like individual particle-particle contact areas and numbers of neighboring particles, can be easily monitored. The downside of the method, on the other hand, are high computational times and, accordingly, a limitation in the number of particles that can be simulated.

The initial particle configuration of a sample representing a dried inkjet-printed line on a rigid substrate was created by a generation scheme as described in detail by Henrich *et al.*[44] Unless otherwise stated in the text, the setup consists of randomly distributed spherical particles of equal sizes. As the lateral dimensions of the line (µm) are about one to three orders of magnitude larger than the line thickness (nm) and the substrate accordingly prevents lateral sinter shrinkage in the line center, fixed periodic boundary conditions were applied in the in-plane-directions (see Figure 1a) to keep the number of particles at a reasonable value. In order to guarantee that opposing sides of the sample do not affect each other over the periodic boundaries, the length in the periodic directions d_{pbc} has to be above a critical lower bound. The height loss of samples with equal line thickness but different values of d_{pbc} ranging from 24 to 48 times the particle diameter have been compared and hardly any difference is observable between the different cases (see exemplarily line thickness and resistivity in ESI Figure 1). Therefore, d_{pbc} is set to 36 times the particle diameter for all simulations, which is seen as a secure choice. For the top surface, free boundary conditions were used, while at the bottom a constraining boundary was imposed by a substrate. The substrate was represented explicitly by particles that have the same properties as the particles used for the line but are fixed during the simulation and, therefore, represent a rigid non-shrinking surface. A representative initial particle configuration with typical dimensions and 35000 particles is shown in Figure 1b.

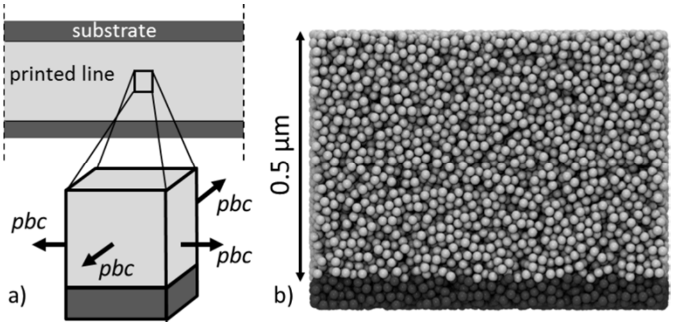

Figure 1. Cutting the simulation sample out of the printed line on a substrate and application of periodic boundary conditions (**a**); reference sample for DEM simulations consisting of about 35000 particles (**b**).

The applied DEM simulation procedure is based on the force calculation of Riedel and Svoboda[45, 46] and is described in detail by Henrich *et al.* [44] Therefore, only the relevant aspects of the method are given here. The DEM sintering method as employed in this work is valid to simulate the initial and intermediate stages of solid-state sintering, i.e. up to relative densities of around 90%, where the assumptions that grain boundary diffusion is the dominant transport mechanism and neighboring contacts do not interact start to become unrealistic.[40, 44] Up to a certain degree, the particles are allowed to overlap in order to simulate neck formation and coalescence during sintering. The normal force between two spherical grains F_n then contains an attractive part F_a and a viscous repulsive part F_v and can be written as:[46]

$$F_n = F_a + F_v = -\gamma_s(2\kappa A + L\sin\psi) + \frac{\pi c^4 k_B T}{8\Omega\,\delta D_b}\, v_n \qquad (1)$$

with γ_s being the specific surface energy, κ the curvature of the surface, $A = \pi c^2$ the grain contact area with radius c, L the length of its perimeter and ψ the dihedral angle. k_B is the Boltzmann constant, T the absolute temperature, Ω the atomic volume and δD_b the grain boundary thickness times the grain boundary diffusion coefficient. The latter product has an Arrhenius type temperature dependence, $\delta D_b = \delta D_{b,0}\exp(-Q_{gb}/R_gT)$, where Q_{gb} is the activation energy for grain boundary diffusion and R_g the universal gas constant. The component of the relative grain-grain velocity perpendicular to the contact area is denoted by $v_{ij}^{\,n}$. Since surface curvature κ in equation (1) is not easily accessible, Henrich propose a description that relates the attractive force F_a to the sintering stress σ_S and the distance d between two particles assuming a body-centered cubic (bcc) grain arrangement: [44, 47]

$$F_a = -\frac{d^2}{\sqrt{3}}\,\sigma_S \qquad (2)$$

In the bcc case, the porosity p can locally be approximated by the fraction of particle volume $V_{part} = 2 \cdot {}^{4}/_{3}\,\pi R^3$ in a bcc primitive cell and the cell volume $V_{cell} = {}^{8d^3}/_{3^{3/2}}$ resulting in:

$$p = 1 - \frac{V_{part}}{V_{cell}} = \; 1 - \pi\sqrt{3}\,\frac{R^3}{d^3} \qquad (3)$$

Moreover, Svoboda *et al.* provide polynomial approximations to numerical solutions for the contact radius c and the sintering stress σ_S:[45]

$$c \approx C(p,\psi) = [0.5998 + 0.0533\,\psi + (-1.271 + 0.04144\,\psi)p] \cdot R$$

$$\begin{aligned}\sigma_S \approx \Sigma(p,\psi) = \; & [(-4.069 + 6.557\,\psi + 0.0253\,\psi^2) \\ & + (26.75 - 42.58\,\psi + 5.986\,\psi^2)p \\ & + (-51.01 + 82.12\,\psi - 18.56\,\psi^2)p^2] \cdot \frac{\gamma_s}{R}\end{aligned}$$

Finally, equation (2) can be rewritten in terms of porosity p (resp. in terms of inter-particle distance d taking into account equation (3)):

$$F_n = -\frac{\pi^{2/3} R \gamma_s}{3^{1/6}(1-p)^{2/3}}\,\Sigma(p,\psi) + \frac{\pi C(p,\psi)^4 k_B T}{8\Omega\,\delta D_b}\,v_n \qquad (4)$$

Additionally, the attractive part of the normal force F_a is set to zero at full density ($p < 0$), whereas $F_n = 0$ holds in the case of no contact between the particles ($d > 2R$).

The total force as well as the total torque acting on a particle is calculated from the sum of particle–particle forces and torques. The temporal evolution of the particle system is governed by Newton's equations of motion using a Velocity-Verlet integration scheme.[44]

3.2 Resistivity computation

For a resistor with uniform cross-section, the resistivity is defined as $\rho = R \cdot A_R / l$ with R being the resistance, l the length and $A_R = h \cdot w$ the cross-section area of the line, where h is the line height and w its width. In the case of a thin film like an inkjet-printed line, resistance changes to sheet resistance R_s since both w and l can be seen as infinitely large compared to h and the formula for resistivity can be rewritten as $\rho = R_s \cdot h$ or $R_s = \rho / h$ respectively. Since the printed line is composed of particles and not of bulk material, it is evident that the resistance must be higher than in the bulk material case. Therefore, an empirical factor $\eta > 1$ is introduced to account for this fact and the sheet resistance for a non-bulk line can be expressed phenomenologically by:

$$R = \eta \cdot \frac{\rho_{bulk}}{h_0} \qquad (5)$$

where ρ_{bulk} is the resistivity of the bulk material and h_0 the initial line height. For the temporal evolution for the factor η the following dependency is assumed:

$$\eta = \begin{cases} \infty & , \; t < t_0 \\ a_1 \cdot \exp\left(a_2 \cdot \dfrac{\lambda}{k \cdot c \cdot \mu}\right) + a_3 \, , & t \geq t_0 \end{cases} \qquad (6)$$

with λ representing the length of the minimum percolation path through the sample measured in particles and normed by the sample length, k the average number of next neighbors of all particles, *i.e.* the coordination number, c the average particle-particle contact radius and μ a percolation topology parameter that is described below. The values a_1, a_2, a_3 are seen as free fitting parameters. The percolation time t_0 defines the time when a continuous path of connected particles is established through the simulation sample for the first time. Obviously, before such a connected path appears, no conductivity through the line is possible, which corresponds to an infinitely high resistance. Here, two particles are said to be electrically connected when the radius of the circular contact area exceeds a certain threshold value c_{min}, which represents implicitly the hampered contact forming due to the existence of remaining organic in the sample. The value c_{min} is also seen as a free fitting parameter. While the coordination number and the average contact radius are directly available from the sintering simulation, an additional procedure has to be performed in order to obtain the percolation values. After each time step, the microstructure calculated by the process simulation is analyzed in order to find a connected path through the sample. For that purpose, one lateral face of the sample is set in contact with a virtual electrode and, therefore, the particles adjacent to the electrode are marked as conductive (see Figure 2). Starting from these particles, contacting particles fulfilling $c > c_{min}$ are detected gradually and tagged as being conductive. In this manner, a path of connected particles can be found. The moment when a continuous path from one side to the opposite side has formed for the first time is set as the percolation time t_0. From this moment on, the number of contacts that have to be passed through each percolation path is determined. The minimum value is then normed by the sample length in conduction direction and set to the minimum percolation path length λ. Moreover, cross-sections are distributed equidistantly over the sample in conduction direction and the fraction $\bar{\mu}$ of particles participating in one or more percolation paths relative to particles that are not participating is detected respectively for each section as illustrated in the sketch of Figure 2. The minimum value of these fractions marks then the bottleneck of the percolation topology and is set as the percolation topology parameter μ.

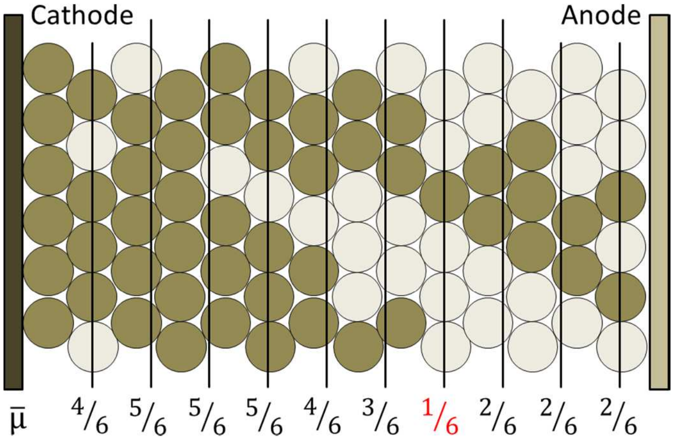

Figure 2. Sketch exemplifying a two dimensional (2D) percolation topology of conductive particles (gray) growing from the cathode towards the anode. Equidistant cross-sections for the determination of the fraction of particles participating in percolation paths $\bar{\mu}$ are also shown. Here, the percolation topology parameter μ is $\min(\bar{\mu}) = 1/6$.

The definition of η is motivated by the fact that a large number of contacts within the percolation path to be passed by electrons evidently leads to a high line resistance. As a consequence, an increased percolation path length λ results in a higher value of the factor η. The topology of all percolation paths is represented by the parameter μ, assuming that the quality of the conductive line is characterized by percolation path bottlenecks. The more pronounced the bottleneck is, the smaller is the value of μ and hence the larger is the factor η. The same correlation holds for the coordination number and the average contact radius, since a small number of contacting neighbors impedes the formation of percolation paths and small contact areas are less likely to let electrons pass from one particle to the other. Combining equation (2) and (3), the final resistivity evolution can then be expressed as:

$$\rho = \begin{cases} \infty & , \ t < t_0 \\ \rho_{bulk} \left(a_1 \cdot \exp\left(a_2 \cdot \dfrac{\lambda}{k \cdot c \cdot \mu} \right) + a_3 \right) \dfrac{h}{h_0} & , \ t \geq t_0 \end{cases} \qquad (7)$$

4. Results and discussion

4.1 Ink characterization

In order to establish a sintering model, a commercial silver NP ink was analyzed regarding metal content, particle size and behavior upon thermal stimuli. Afterwards thermal sintering at 175 °C was performed and the obtained lines were investigated regarding electrical properties, mass loss behavior, grain size development and material densification. Furthermore, the correlation between mass loss, height loss of printed structures, grain size and electrical resistivity was investigated in order to gain further understanding of the process of NP sintering. The data on thermal sintering at 175 °C was then used to establish a sintering model and to predict the resistivity at 150 and 200 °C, respectively. These results were finally compared with experimental data produced at these temperatures.

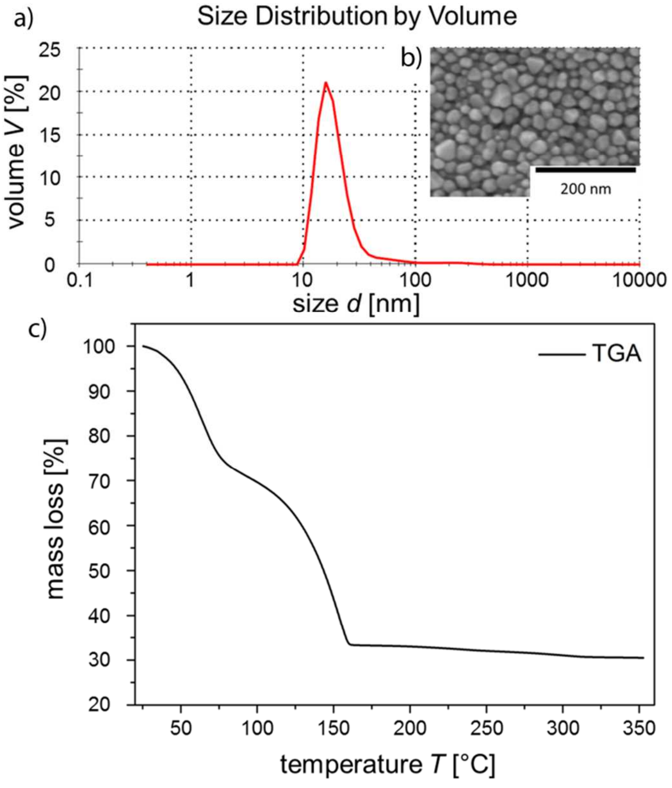

Figure 3. Particle size investigations by dynamic light scattering (DLS) (**a**) and scanning electron microscopy (SEM) (**b**); mass-loss investigation by thermogravimetric analysis (TGA) with the application of a temperature ramp of 10 K min^{-1} (**c**).

At first, the aqueous silver ink was investigated regarding particle size, metal content and mass loss upon thermal stimuli. Dynamic light scattering (DLS) analysis and scanning electron microscopy (SEM) of the unsintered ink (Figure 3a, b) reveal an average particle radius of approximately 10 nm. Thermogravimetric analysis (TGA) between 25 and 350 °C shows two major mass losses in the temperature range of 50 to 60 °C as well as in the range of 120 to 150 °C, which can be attributed to the evaporation of the low and high boiling solvents from the ink, respectively (Figure 3c). Above 160 °C, there is a slight continuous mass loss, which can be attributed to a slow and steady decomposition of the stabilizing molecules at higher temperatures. The ink has an overall solvent content of 66%, a total silver content of 30.5 % and a total stabilizer content of 3.5%.

4.2 Experimental results of thermal sintering at 175 °C

In order to obtain experimental data that can be used as input for a sintering simulation, thermal sintering of inkjet-printed lines was conducted at 175 °C. During thermal sintering, the deposited ink was kept at a constant temperature for a defined amount of time. To investigate the behavior of this ink during thermal sintering, isothermal TGA was performed at 175 °C. For a quantification of the mass losses due to polymeric stabilizer degradation and to exclude mass loss effects of residual solvent, the ink was dried prior to TGA. Figure 4 (red line) shows a slow and steady mass loss of the stabilizing polymer over sintering time rather than an immediate stabilizer decomposition. From the mass losses obtained from isothermal TGA and a total amount of stabilizing polymer of 10.3% (dry ink), the mass loss of the polymer itself was calculated for selected sintering times (Table 1).

Table 1. Mass loss and resistivity at selected sintering times at a sintering temperature of 175 °C.

	Mass loss stabilizer / %	ρ / µΩ·cm
5 min	5.4	8.7
10 min	6.6	4.2
30 min	12.0	4.0
60 min	18.7	4.2

It can be observed that it is not possible to completely remove the polymeric stabilizer from the ink. In fact, after 60 minutes less than 20% of total amount of polymeric stabilizer is removed from the ink. The resistivity development during thermal sintering at 175 °C is also shown in Figure 4 (black line and squares). In contrast to the mass loss behavior, the resistivity decreases to values around 4.0 µΩ·cm after 10 min of sintering and does not decrease with longer sintering times. Table 1 and Figure 4 compare the development of polymer dedicated mass loss and arising resistivity. Whereas resistivity values decrease to 8.7 µΩ·cm and 4.2 µΩ·cm after 5 and 10 min respectively, a rather low mass loss of 5.4% to 6.6% is observed in this time frame. It is therefore possible to create conductive structures with more than 90% of the insulating stabilizer still present in the deposited material. Moreover, the polymer dedicated mass loss persists for longer sintering times whereas the resistivity values reach a plateau already after 10 minutes, indicating that the process of sintering is completed. From these results it can be concluded that the removal of insulating stabilizer has a minor impact to the obtainable resistivity at a sintering temperature of 175 °C, which is in agreement to the observation Volkman *et al.*.[36] It should be noted that many polymeric stabilizers used in silver NP inks (for example, PAA, PVP) have glass transition temperatures below 150 °C. Above their glass transition temperature, these polymers are flexible and allow migration of the polymers themselves as well as the silver NPs. It suggests that the organic stabilizer might no longer be present in-between the particles but have been desorbed from the NPs surface at increased temperatures.

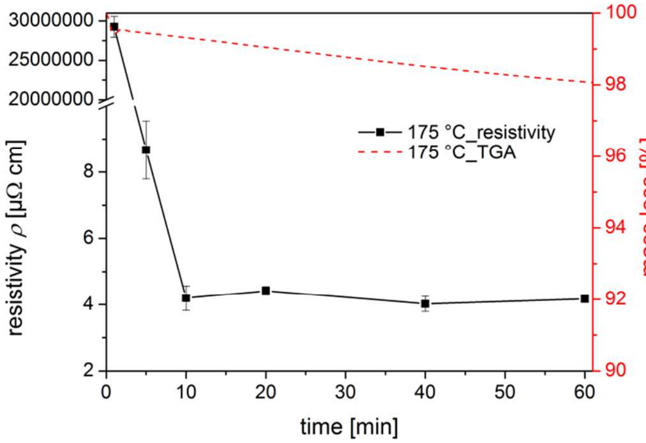

Figure 4. Isothermal thermogravimetric analysis (TGA) of vacuum dried ink (**red dotted line**) and resistivity (*ρ*) development over sintering time (*t*) (**black solid line and squares**) at a sintering temperature of 175 °C.

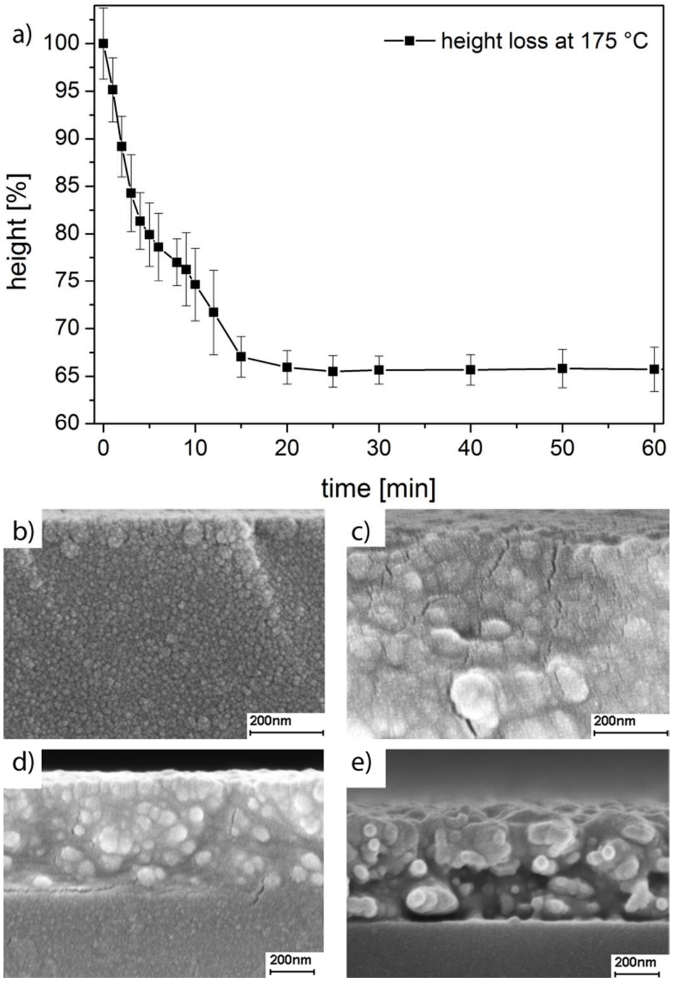

Figure 5. Height loss (*h*) of printed lines during sintering at 175 °C (**a**), scanning electron microscopy (SEM) of the cross-sections of as printed ink (**b**) and thermally sintered ink at 175 °C for 2 min (**c**), 10 min (**d**) and 60 min (**e**), respectively.

The densification of the printed silver ink during thermal sintering was investigated by measuring the line height after each sintering time (Figure 5a). The line height decreases to roughly 65% of its original value within the first 10 to 15 min of sintering. For longer sintering times the lines stay at this height indicating again the completion of the sintering process at 175 °C. Height loss behaves similar to the resistivity development and reaches a plateau whereas polymer mass loss (from TGA) persists. The height loss of 35% is more likely due to densification by clustering and grain growth of the silver particles.

SEM investigation of the cross-section of inkjet-printed lines shows the grain size development during thermal sintering (Figure 5b to e). It could be observed that the discrete particles in the as-printed ink form clusters and larger particles already after 2 min of sintering (Figure 5c). Due to the energy input from the elevated temperatures, neck formation and the formation of a densely packed silver network occurs. However, after a sintering time of 60 min at 175 °C (Figure 5e) the structure still possesses cavities and is porous enough to contain the remaining 80% of polymeric stabilizer. Due to the minor correlation of resistivity and removal of the stabilizer, the decomposition of the organic shell was not considered explicitly in the sintering model but only by introducing the heuristic parameter c_{min} (see section 3.2). This minimum contact radius threshold represents the existence of organic matter in the line that prevents adjacent particles from letting electrons pass through the contact area and consequently impedes the formation of percolation paths artificially, although sintering occurs from the beginning on. Hence, this heuristic reproduces the behavior observed in the experiments, where a height loss due to sintering can be measured from the start but resistivity just after an inhibition time.

4.3 Simulation of thermal sintering

The two-stage model described in section 3 was applied to compute the temporal evolution of electrical resistivity of thermally sintered lines.

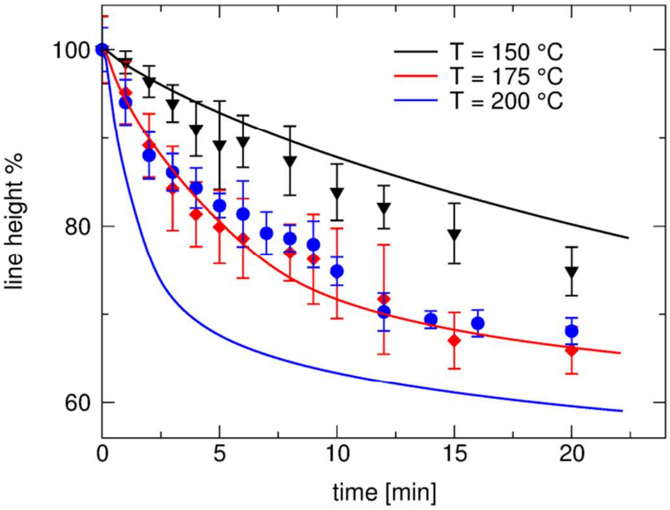

Figure 6. Simulated (**lines**) and measured (**dots**) line height decrease during sintering of an inkjet-printed NP ink at 150 °C (**black triangles**), 175 °C (**red squares**) and 200 °C (**blue circles**). A free simulation parameter was fit according to the experimental data for 175 °C.

The model contains free parameters that have to be adapted in order to fit the experimental results. For that purpose, the experimental height loss data obtained for 175 °C was used to calibrate the process model (stage 1) by taking the parameter values from Table 2 and adapting $\delta D_{b,0}$. Each simulation was repeated three times with different randomly distributed particle configurations. Simulations with $\delta D_{b,0}$ = 5.8 × 10^{-19} m^3/s show good accordance with the experimental data regarding to line height decrease, as can be seen in Figure 6.

Table 2. DEM simulation parameters for the sintering of an inkjet-printed silver line. The values for γ_s, Ω, and Q_{gb} were taken from reference,[48] r and h_0 were set according to the experimental conditions mentioned above.

Particle radius r	10 nm
Initial line height h_0	0.5 µm
Surface energy γ_s	1.12 J/m^2
Dihedral angle ψ	π/3 (60°)
Atomic volume Ω	1.71 × 10^{-29} m^3
Activation energy for grain boundary diffusion Q_{gb}	89.8 kJ/mol
Grain-boundary thickness times diffusion coefficient $\delta D_{b,0}$ (fitting parameter)	5.8 × 10^{-19} m^3/s

Taking this final parameter set given in Table 2, the components of the normal force interacting between two grains according to equation (4) are illustrated in Figure 7 as a function of inter-particle distance d for T = 175°C and an exemplary constant normal relative grain-grain velocity v_n = 5.0x10^{-12} m/s. It shows that the total force is attractive (negative) up to a certain particle-particle approach where the repulsive viscous part F_v exceeds the attractive part F_a. It has to be noted that v_n is not constant in a real simulation but varies according to the acting normal force, which leads to a permanent shift of the equilibrium point where the normal force is zero.

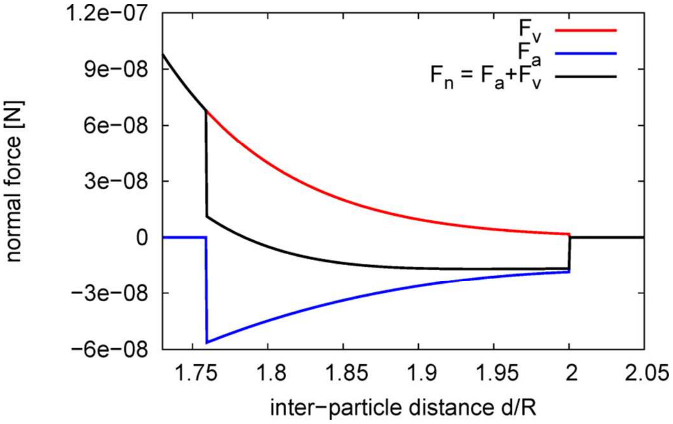

Figure 7. Attractive (F_a) and repulsive (F_v) normal force acting between two particles as a function of inter-particle distance using the parameters from Table 2 with T = 175°C and v_n = 5.0x10^{-12} m/s.

The development of the inter-particle normal force averaged over all contacts for this simulation setup is shown in Figure 8 indicating that the maximum total force is reached at about 9 minutes and afterwards it tends to level at a plateau in the attractive force regime. This is due to the interaction with the substrate, which introduces tensile stresses in lateral directions and, therefore, impedes that the particles in the film are in a force free mechanical equilibrium. The complete system (film and substrate together), however, is going to reach an equilibrium, at least after long time sintering, which is also indicated by the saturation of the line height loss in Figure 6.

Subsequently, simulations with the same parameters and different temperatures (150 and 200 °C, respectively) have been performed and compared to the experimentally obtained values, revealing again good accordance for 150 °C which is seen as a validation of the sintering process model. As far as the experimental data for 200 °C is concerned, a comparison is complicated since unexpectedly it does not show any significant differences to the measurements at 175 °C. The reasons for the unexpected height development at 200 °C compared to 175 °C is currently unknown and has to be investigated in further detail. Possible reasons for these deviations might be the non-consideration of the polymer decomposition as well as experimental measurement inaccuracies. In particular, the experimental height determination had to be performed in short intervals in the first 15 minutes of sintering, which required several short heating steps. This results in temperature inaccuracies due to heating up, whereas in the simulations an ideal isothermal temperature was considered.

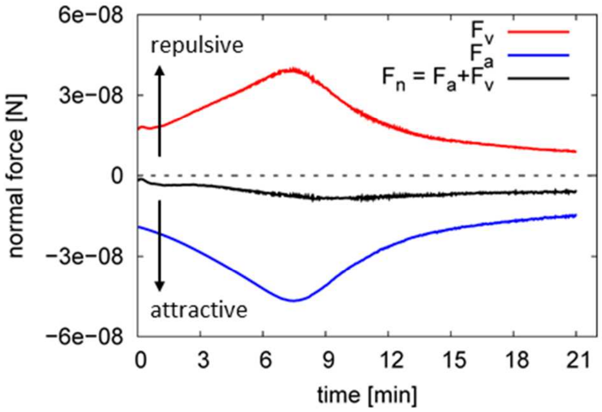

Figure 8. Temporal development of inter-particle normal force averaged over all contacts.

The DEM sintering simulation provides information about the microstructure evolution of the particle assemblies, from which the required parameters for the resistivity computation in equation (4) can be extracted as pointed out in section 3. The temporal evolution of these parameters is given in Figure 9 for the three sintering temperatures.

Equation (4) includes a_1, a_2 and a_3 and implicitly the minimum contact radius c_{min} as free parameters that have to be adapted to experimental findings. These parameters have been fit with the help of the resistivity data obtained experimentally at 175 °C. The results of the fitting procedure are given in Table 3. Figure 10 shows the computed resistivity evolution together with the experimental data. Again, the computation was repeated for other temperatures using the parameter set determined for 175 °C and is compared with experimental measurements in order to validate the resistivity model in equation (4). The moment when the resistivity drops matches quite well for all temperatures. However, the simulated resistivity is underestimated in the first minutes in the case of 200 °C, which correlates with the overestimated height loss at this temperature as shown in Figure 6.

The final computed resistivity values, however, follow the gradation observed in the experiment, *i.e.* the higher the sintering temperature, the lower is the final resistivity. Using the simulations, final resistivity values of 2.2× bulk silver at 200 °C after 20 min, 2.7×bulk at 175 °C after 20 minutes and 3.4×bulk at 150 °C after 30 minutes. The simulated results are in good agreement with the experimental values, which are in the range of 1.9×bulk (200 °C), 2.8×bulk (175 °C) and 3.1×bulk (150 °C) bulk silver resistivity (ESI Table 1 and ESI Figure 2). Furthermore, the finding of the minor influence of stabilizer decomposition during thermal sintering at 175 °C was confirmed for sintering at 150 and 200 °C, respectively. The comparison of stabilizer dedicated mass loss and achieved resistivity shows an ongoing mass loss after the lowest resistivity has been reached.

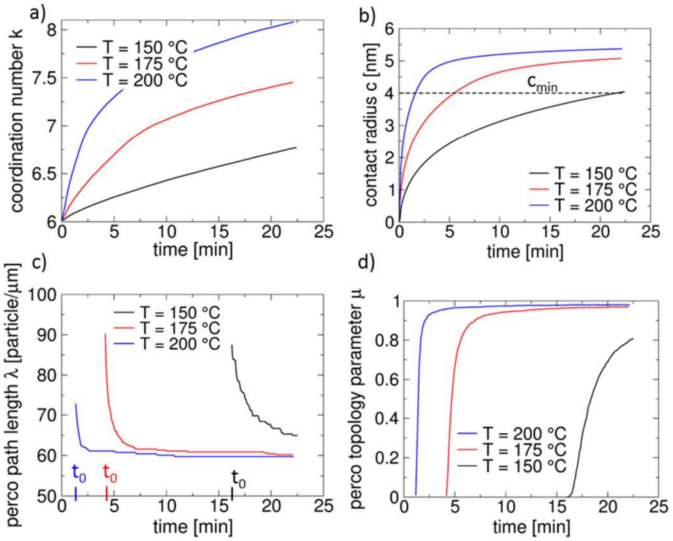

Figure 9. Temporal evolution of parameters needed for the resistivity model that are extracted from sintering simulation: Average coordination number k (**a**); average contact radius c (the dashed line indicates c_{min} = 4 nm) (**b**); length of minimum percolation path λ (including percolation times t_0) (**c**); percolation topology parameter μ (**d**). A description of these parameters can be found in section 3.2.

Table 3. Values for the free parameters in resistivity equation (4) adapted to experimental data at 175 °C.

c_{min}	a_1	a_2	a_3
4 nm	198.0	5.35×10^{-18} m^2	-195.8

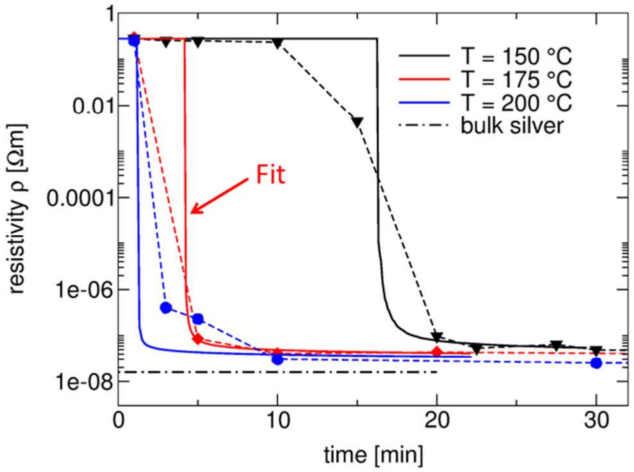

Figure 10. Comparison of resistivity measured in experiment (**dots**) and computed by equation 4 (**solid lines**) with parameters fitted to data for 175 °C.

A comparison of resistivity values and corresponding stabilizer decomposition is given in ESI Table 1. Furthermore, the resistivity of inkjet-printed lines is not directly dependent on the stabilizer mass loss. At 150 °C, a resistivity of 5 µΩ·cm was reached after 30 minutes with 8.3% of the stabilizer removed from the printed material. On the other hand, 5 min sintering at 200 °C removes significantly more organic material from the ink (13.1%) while revealing a higher resistivity of 23.1 µΩ·cm. Volkman *et al.*[36] described a similar behavior of thiol stabilized silver NPs, where sintering temperatures well below the decomposition temperatures of the organic stabilizers were sufficient to detach the organic shell from the particles.

4.4 Parameter variations

After validating the model, further simulation has been performed at the reference temperature of 175 °C with varying particle sizes and different particle size distributions while all other parameters were kept unchanged. For the particle size variation, line height has been changed to 1 µm to guarantee the presence of a sufficient number of particles in thickness direction also for larger particles that is necessary for reasonable conclusions. Figure 11 shows the resistivity evolution for samples with particles with radiuses of 10, 15 and 20 nm, respectively. As can be seen, the particle size affects the percolation time at which a finite resistivity can be measured remarkably for the initial stage of sintering. The reason for this is the same as for the observations regarding temperature variation, *i.e.* larger particles (as well as low temperatures) delay the sintering process[47], an effect that is shown in Figure 11c, where the height loss is plotted as a representation of sintering densification. This delay leads to a hampering of contact area formation (see Figure 11d) and the minimum contact radius for connectivity of two particles c_{min} is passed later. Figure 11b shows that the final resistivity increases as well with increasing particle size at least in the investigated time range. As Figure 11d shows, the contact area between two particles of larger size exceeds the one for the case of particles with small particle sizes after a certain while. This leads to the assumption that a long-time observation would show the resistivity in the case of large particles falling below that of small particles. This assumption, however, cannot be proved since only the first 20 minutes have been simulated due to very high computation times and the interest of industry in short-time production processes.

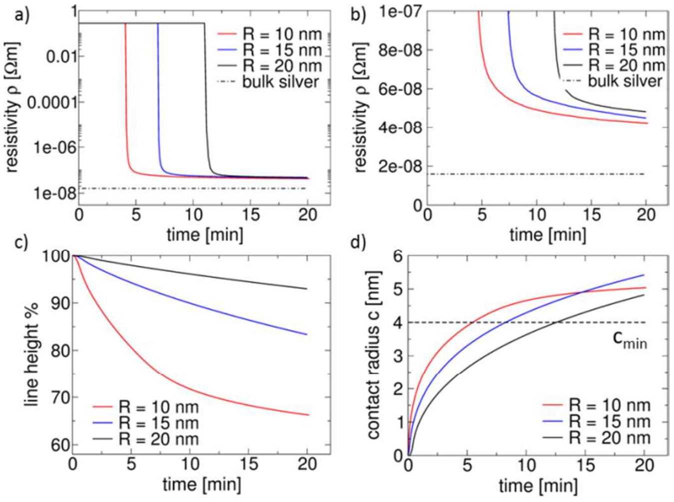

Figure 11. Computed resistivities for lines composed of particles with different sizes at a sintering temperature of 175 °C with logarithmic scaling (**a**) and zoomed into the resistivity range of interest (**b**), line height decrease (**c**) and contact radius evolution (**d**).

In order to analyze the effect of a particle size distribution on resistivity development, the existing samples with equally sized particles of radius of 10 nm were compared with samples that consist of particles with log-normal distributed sizes (mean radius 10 nm, standard deviations of $\sigma = 0.1$ and $\sigma = 0.2$).[49] Since the mean radius is equal within this variation, sintering densification is similar (see Figure 12a) and the percolation times coincide (Figure 12b). The resistivity evolution shown in Figure 12c, however, shows a slight tendency to smaller resistivity values for higher σ. This may be due to facilitated particle rearrangement in the case of broader particle size distributions because of the presence of small particle that are less bonded and fit into gaps that exist in the packing and, therefore, enhance the formation of percolation paths. On the other hand, since line height loss and percolation time do not show a significant difference, another effect is more likely to be the cause of this observation, which is the evolution of the minimum length of the percolation paths λ. As indicated in Figure 12b, it is the lower for broader particle size distributions. The reason for this is that in the case of a broad distribution a certain amount of large particles are available that can form a connected particle chain through the sample that is shorter than in the case of narrow particle size distributions, where all particles are as small as the mean radius.

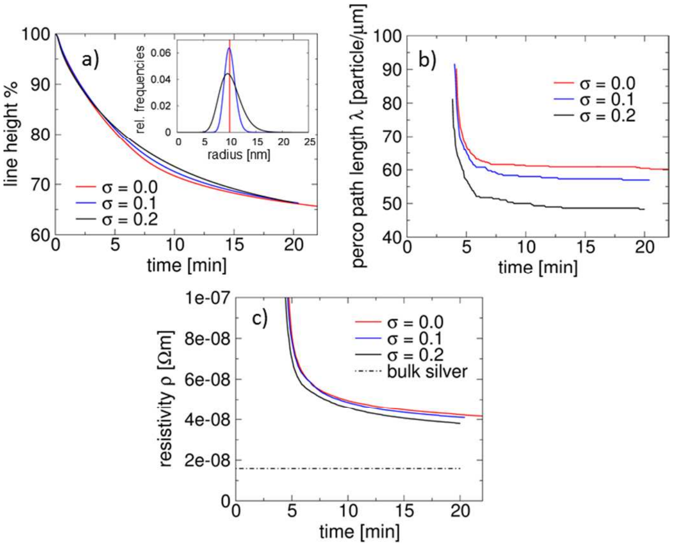

Figure 12. Line height decrease for samples with different particle size distributions (inset) at a sintering temperature of 175 °C (**a**), minimum length of percolation paths (**b**) and resistivity evolution of these setups (**c**).

5. Conclusions

In summary, a simple model has been developed for the computation of resistivity evolution in an inkjet-printed silver line during isothermal sintering. Its key feature is the fact that for a new ink free parameters in the model have to be determined only once for an appropriate reference temperature. Subsequently, the model can predict the results for other temperatures (at least in a certain range around the reference temperature) and for the variation of other properties, which are often hardly accessible in experiment. The calibration as well as the validation of the model were achieved with the help of experimental data, where the sintering behavior of an inkjet-printed NP ink and relevant properties like particle size, mass loss during isothermal heating, height loss as well as resistivity development are recorded. Resistivity values in the range of 3.1 to 1.9 times bulk silver were obtained after 30 minutes of sintering at temperatures between 150 and 200 °C. The comparison of resistivity data and stabilizer dedicated mass loss during isothermal heating revealed that the decomposition of the polymeric stabilizer has only a minor impact on the resistivity of an inkjet-printed line and was, therefore, excluded from the derived model.

Additional parameter studies have been performed showing that applying small particles with a broad particle size distribution and high sintering temperatures are, in general, beneficial in order to obtain a low resistivity, which is requested for industrial applications. Although the resistivity model is kept quite simple, it could be applied to other silver NP based inks to investigate the resistivity development with different temperature profiles and processing times. To do so, only experimental input data of one reference temperature, *i.e.* height loss and resistivity development, is needed, for which the free model parameters will be calibrated.

The variation and addition of processing parameters also opens the way of alterations of the here described model to be used for alternative sintering approaches, like photonic sintering, in order to compare the predicted resistivity results of different sintering technologies. Since the metal ink development aims for cheaper materials like copper, the model can be applied to inks composed of other materials but silver as well, for which, however, a recalibration of the fitting parameters with help of experimental data is very likely to be required.

Acknowledgements

For financial support the authors thank the Dutch Polymer Institute (DPI, technology area HTE) as well as the European Community's Seventh Framework Programme (FP7/2007-2013) LOTUS under grant agreement n° 248816. Furthermore, the authors express their gratitude to Steffi Stumpf from the Friedrich Schiller University Jena, Germany for providing SEM images.

References

1. B. J. de Gans, P. C. Duineveld and U. S. Schubert, *Adv. Mater.*, 2004, **16**, 203-213.
2. G. Cummins and M. P. Y. Desmulliez, *Circuit World*, 2012, **38**, 193-213.
3. J. B. Szczech, C. M. Megaridis, D. R. Gamota and J. Zhang, *IEEE T. Electron. Pack.*., 2002, **25**, 26-33.
4. J. Perelaer and U. S. Schubert, *J. Mater. Res.*, 2013, **28**, 564-573.
5. J. Perelaer, P. J. Smith, D. Mager, D. Soltman, S. K. Volkman, V. Subramanian, J. G. Korvink and U. S. Schubert, *J. Mater. Chem.*, 2010, **20**, 8446-8453.
6. V. Subramanian, J. M. J. Fréchet, P. C. Chang, D. C. Huang, J. B. Lee, S. E. Molesa, A. R. Murphy, D. R. Redinger and S. K. Volkman, *P. IEEE*, 2005, **93**, 1330-1338.
7. F. C. Krebs, *Org. Electron.*, 2009, **10**, 761-768.
8. H. M. Haverinen, R. A. Myllyla and G. E. Jabbour, *J. Disp. Technol.*, 2010, **6**, 87-89.
9. K. Woo, C. Bae, Y. Jeong, D. Kim and J. Moon, *J. Mater. Chem.*, 2010, **20**, 3877-3882.
10. S. Wünscher, B. Seise, D. Pretzel, S. Pollok, J. Perelaer, K. Weber, J. Popp and U. S. Schubert, *Lab Chip*, 2014, **14**, 392-401.
11. J. C. Batchelor, E. A. Parker, J. A. Miller, V. Sanchez-Romaguera and S. G. Yeates, *Electron. Lett.*, 2009, **45**, 7-8.
12. P. J. Smith, D. Y. Shin, J. E. Stringer, B. Derby and N. Reis, *J. Mater. Sci.*, 2006, **41**, 4153-4158.

13. Z. C. Liu, Y. Su and K. Varahramyan, *Thin Solid Films*, 2005, **478**, 275-279.
14. T. H. J. van Osch, J. Perelaer, A. W. M. de Laat and U. S. Schubert, *Adv. Mater.*, 2008, **20**, 343-345.
15. D. Huang, F. Liao, S. Molesa, D. Redinger and V. Subramanian, *J. Electrochem. Soc.*, 2003, **150**, G412-G417.
16. A. Kamyshny, J. H. G. Steinke and S. Magdassi, *Open Appl. Phys. J.*, 2011, **4**, 19-36.
17. S. Magdassi, A. Bassa, Y. Vinetsky and A. Kamyshny, *Chem. Mater.*, 2003, **15**, 2208-2217.
18. J. Perelaer, A. W. M. de Laat, C. E. Hendriks and U. S. Schubert, *J. Mater. Chem.*, 2008, **18**, 3209-3215.
19. J. H. Yao, K. R. Elder, H. Guo and M. Grant, *Physica A*, 1994, **204**, 770-788.
20. R. S. Goeke and A. K. Datye, *Top. Catal.*, 2007, **46**, 3-9.
21. H. H. Lee, K. S. Chou and K. C. Huang, *Nanotechnology*, 2005, **16**, 2436-2441.
22. J. Perelaer, B.-J. de Gans and U. S. Schubert, *Adv. Mater.*, 2006, **18**, 2101-2104.
23. I. Reinhold, C. E. Hendriks, R. Eckardt, J. M. Kranenburg, J. Perelaer, R. R. Baumann and U. S. Schubert, *J. Mater. Chem.*, 2009, **19**, 3384-3388.
24. S. Wünscher, S. Stumpf, A. Teichler, O. Pabst, J. Perelaer, E. Beckert and U. S. Schubert, *J. Mater. Chem.*, 2012, **22**, 24569-24576.
25. S. H. Ko, H. Pan, C. P. Grigoropoulos, C. K. Luscombe, J. M. J. Fréchet and D. Poulikakos, *Appl. Phys. Lett.*, 2007, **90**, 141103.
26. T. Kumpulainen, J. Pekkanen, J. Valkama, J. Laakso, R. Tuokko and M. Mäntysalo, *Opt. Laser Technol.*, 2011, **43**, 570-576.
27. H. S. Kim, S. R. Dhage, D. E. Shim and H. T. Hahn, *Appl. Phys. A-Mater.*, 2009, **97**, 791-798.
28. G. L. Allen, R. A. Bayles, W. W. Gile and W. A. Jesser, *Thin Solid Films*, 1986, **144**, 297-308.
29. L. H. Liang, C. M. Shen, S. X. Du, W. M. Liu, X. C. Xie and H. J. Gao, *Phys. Rev. B*, 2004, **70**, 205419.
30. J. Perelaer, A. W. M. de Laat, C. E. Hendriks and U. S. Schubert, *J. Mater. Chem.*, 2008, **18**, 3209-3215.
31. D. Wakuda, K.-S. Kim and K. Suganuma, *IEEE T. Comp. and Package. Technol.*, 2009, **32**, 627-632.
32. M. J. Coutts, M. B. Cortie, M. J. Ford and A. M. McDonagh, *J. Phys. Chem. C*, 2009, **113**, 1325-1328.
33. S. Magdassi, M. Grouchko, O. Berezin and A. Kamyshny, *ACS Nano*, 2010, **4**, 1943-1948.
34. M. Grouchko, A. Kamyshny, C. F. Mihailescu, D. F. Anghel and S. Magdassi, *ACS Nano*, 2011, **5**, 3354-3359.
35. Y. Tang, W. He, G. Zhou, S. Wang, X. Yang, Z. Tao and J. Zhou, *Nanotechnology*, 2012, **23**.
36. S. K. Volkman, S. Yin, T. Bakhishev, K. Puntambekar, V. Subramanian and M. F. Toney, *Chem. Mat.*, 2011, **23**, 4634-4640.
37. H. A. Alarifi, M. Atis, C. Özdoğan, A. Hu, M. Yavuz and Y. Zhou, *Mater. Trans.*, 2013, **54**, 884-889.
38. L. J. Lewis, P. Jensen and J. L. Barrat, *Phys. Rev. B*, 1997, **56**, 2248-2257.
39. P. A. Cundall and O. D. L. Strack, *Geotechnique*, 1979, **29**, 47-65.
40. A. Wonisch, O. Guillon, T. Kraft, M. Moseler, H. Riedel and J. Roedel, *Acta. Mater.*, 2007, **55**, 5187-5199.
41. C. L. Martin and R. K. Bordia, *Acta. Mater.*, 2009, **57**, 549-558.
42. T. Rasp, C. Jamin, A. Wonisch, T. Kraft and O. Guillon, *J. Am. Ceram. Soc.*, 2012, **95**, 586-592.
43. L. C. R. Schneider, C. L. Martin, Y. Bultel, D. Bouvard and E. Siebert, *Electrochim. Acta*, 2006, **52**, 314-324.
44. B. Henrich, A. Wonisch, T. Kraft, M. Moseler and H. Riedel, *Acta. Mater.*, 2007, **55**, 753-762.
45. J. Svoboda, H. Riedel and H. Zipse, *Acta. Metall. Mater.*, 1994, **42**, 435-443.
46. H. Riedel, H. Zipse and J. Svoboda, *Acta. Metall. Mater.*, 1994, **42**, 445-452.
47. B. Henrich, *Ph.D. thesis*, Albert-Ludwigs-Universität Freiburg, Freiburg, Germany, 2007.
48. F. B. Swinkels and M. F. Ashby, *Acta. Metall.*, 1981, **29**, 259-281.
49. A. Wonisch, T. Kraft, M. Moseler and H. Riedel, *J. Am. Ceram. Soc.*, 2009, **92**, 1428-1434.

Table of Contents / Graphical Abstract

An aqueous silver nanoparticle ink was studied for its thermal sintering behavior using simulations and experiments. The experiments at 175 °C were used as input for the model, from which the sintering results at other temperatures were predicted and experimentally verified.